A FIRST ESTIMATE OF RADIO HALO STATISTICS FROM LARGE-SCALE COSMOLOGICAL SIMULATION

P. M. Sutter
Department of Physics, University of Illinois at Urbana-Champaign, Urbana, IL 61801-3080

P. M. Ricker
Department of Astronomy, University of Illinois at Urbana-Champaign, Urbana, IL 61801
National Center for Supercomputing Applications, University of Illinois at Urbana-Champaign, Urbana, IL 61801
Draft version October 14, 2011

ABSTRACT

We present a first estimate based on a cosmological gasdynamics simulation of galaxy cluster radio halo counts to be expected in forthcoming low-frequency radio surveys. Our estimate is based on a FLASH simulation of the ΛCDM model for which we have assigned radio power to clusters via a model that relates radio emissivity to cluster magnetic field strength, intracluster turbulence, and density. We vary several free parameters of this model and find that radio halo number counts vary by up to a factor of two for average magnetic fields ranging from 0.2 to 3.1 μG. However, we predict significantly fewer low-frequency radio halos than expected from previous semi-analytic estimates, and we find that upcoming surveys will have difficulty distinguishing models because of large uncertainties and low number counts. Additionally, we find that expected number counts can be degenerate with both re-acceleration and hadronic secondary models of cosmic ray generation. We find that relations between radio power and mass and X-ray luminosity may be used to distinguish models, and by building mock radio sky maps we demonstrate that surveys such as LOFAR may have sufficient resolution and sensitivity to break this model degeneracy by imaging many individual clusters.

Subject headings: cosmology:theory, structure formation, methods: N-body simulations, clusters of galaxies

1. INTRODUCTION

Although diffuse radio halos were discovered in clusters of galaxies more than 50 years ago (Large et al. 1959), complete statistical information about them has only been forthcoming within the past decade, owing to their rarity, steep spectra, and low surface brightnesses. Radio surveys using the Very Large Array (VLA) (Giovannini 1999; Cohen et al. 2007; Giovannini 2009), the Westerbork Synthesis Radio Telescope (WSRT) (Kempner & Sarazin 2001), and the Giant Metrewave Radio Telescope (GMRT) (Brunetti et al. 2007) have detected ~ 20 radio halos at redshifts up to $z \sim 0.4$, along with a variety of smaller-scale radio features in clusters (Kempner et al. 2004). Only about 1/3 of massive ($> 10^{15}\ M_\odot$) clusters are known to host radio halos, and the halos themselves are not associated with any particular member galaxy, but rather dispersed throughout the intracluster medium (ICM) (Feretti et al. 2004). For clusters that do host halos, strong correlations are seen between radio power and X-ray luminosity (Liang et al. 2000; Bacchi et al. 2003; Cassano et al. 2006; Brunetti et al. 2007), halo mass (Cassano et al. 2006), and gas velocity dispersion (Cassano et al. 2008). Also, observations indicate a strong connection between the presence of a halo and morphological evidence for recent mergers (Buote 2001; Brunetti et al. 2009), although some exceptions do exist (Russell et al. 2011). Indeed, recent simulations of merging clusters suggest that the fraction of turbulent clusters is roughly equal to the fraction of clusters hosting radio halos (Vazza et al. 2011).

Electronic address: psutter2@illinois.edu
Electronic address: pmricker@illinois.edu

The proximate cause of diffuse radio halos is most likely synchrotron emission by high-energy electrons in galaxy cluster magnetic fields, but the means of generating and accelerating these electrons remains an open question, since these electrons have relatively short (~ 0.1 Gyr) lifetimes. Dennison (1980) proposed that cosmic ray (CR) electrons are produced as secondary particles by collisions of > 1 GeV cosmic ray protons with ambient thermal ICM protons. The CR protons can be accelerated by shocks and quickly (< 1 Gyr) diffuse throughout the cluster; because of their larger mass, they have much longer synchrotron lifetimes than the electrons. This naturally explains the diffuse, cluster-wide properties of radio halos (Blasi 1999; Pfrommer et al. 2008). Keshet & Loeb (2010) discuss a way in which the correlation between radio and X-ray surface brightness can be explained by hadronic secondary-type models, although this approach requires an extremely strong magnetic field ($\sim 5\ \mu$G at radii ~ 1 Mpc for $z = 0.2 - 0.4$). Gamma-ray observations place limits on the abundance of high-energy protons, since in addition to producing charged pions that decay into the secondary electrons, the proton-proton collisions produce neutral pions, which decay into gamma-ray photons (Blasi & Colafrancesco 1999; Wolfe et al. 2008). These observations indicate that hadronic cosmic rays may contribute at most 5-10 % of the total pressure support in clusters (Ackermann et al. 2010). However, the hadronic secondary model may have difficulty explaining the diminishing of radio power with radius within the Coma cluster and the scaling of radio power with X-ray luminosity (Donnert et al. 2010a,b). Also, the ability of the high-energy protons to stream away from their sources can have significant implica-

tions for the resulting radio emission (Enßlin et al. 2011). While gamma-ray observations have not strictly ruled out this model, recent estimates indicate a tension between the magnetic field strengths required for this scenario and those observed in clusters (Jeltema & Profumo 2011).

Another promising explanation for the acceleration of the cosmic ray electrons is second-order Fermi acceleration by intracluster turbulence (Schlickeiser et al. 1987; Petrosian 2001; Brunetti & Lazarian 2011). The cosmic rays themselves must be injected into the ICM by radio galaxies (Jaffe 1977) or accelerated by merger shocks. Since the lifetime of synchrotron-emitting GeV electrons in the intracluster magnetic field ($\langle B \rangle \sim 1 - 10 \ \mu$G) is at most ~ 0.1 Gyr (Kuo et al. 2004; Brunetti et al. 2009), these electrons must be re-accelerated by some process that operates in a more diffuse fashion. Hence a local acceleration mechanism is favored. The existence of some steep-spectrum low-frequency radio halos may support the re-acceleration model, since the spectral index of the re-accelerated electrons depends on the turbulent Mach number (Brunetti et al. 2008), although future low-frequency surveys are necessary to fully test this picture. Assuming that ICM turbulence locally accelerates cosmic rays to produce clusterwide radio halos, we expect that the radio emission should correlate spatially with the turbulent pressure $\langle \rho v^2 \rangle$. Indeed, this expectation is consistent with observations using Chandra temperature maps (Govoni et al. 2004). However, the fraction of CR electrons that are reaccelerated primaries rather than hadronic secondaries remains to be determined.

Within the next decade and a half the number of known radio halos should increase dramatically owing to the development of sensitive low-frequency radio surveys based on technology originally developed for cellular communications. Examples of the operating and planned instruments include the LOw Frequency ARray (LOFAR), GMRT, the Karoo Array Telescope (KAT), and the Square Kilometer Array (SKA). LOFAR, for example, will be sensitive to radio frequencies between 20 and 240 MHz and will be able to detect sources as faint as $0.4 - 110$ mJy at $15 - 240$ MHz (Jarvis 2007; Röttgering 2003; Röttgering et al. 2006). These characteristics are ideal for detecting and counting radio halos such as the Coma radio halo ($\sim$640 mJy at 1.4 GHz with a spectral index $\sim 0.4 - 0.75$; Deiss et al. 1997) as far away as a redshift of 0.75. Moreover, if the CR electron population is dominated by reaccelerated primaries, then many more radio halos may be detected at low frequencies owing to their steep spectra (Cassano et al. 2008).

Counts of cluster radio halos, in addition to probing the evolution of cluster merger activity, also potentially provide an additional means for using clusters to constrain cosmological parameters. Unlike other methods for using clusters as cosmological probes that are based on their mass function or gas fraction, this measure is linked to their "instantaneous" formation activity rather than their time-integrated numbers. In principle its dependence on the cosmological volume element dV/dz and the growth factor of linear density fluctuations $D_+(z)$ should also be different from and thus complementary to the more traditional measures. Additionally, if the cosmic-ray electrons responsible for the halos are accelerated by shocks and/or turbulence generated by mergers,

it is reasonable to expect that recently merged clusters would display the most radio activity. Thus determining the abundances, spectral distributions, and other characteristics of radio halos as functions of redshift could provide information about the evolution of clusters and their merging activity over time.

In this paper we present results from a numerical simulation of cluster formation intended to study the form and evolution of the radio halo population as might be observed in a typical LOFAR survey. We apply a model of radio power that is generalized to include both hadronic and re-acceleration cosmic ray generation mechanisms. We specifically choose this model to be as broad possible to allow immediate comparisons based on the same simulation. The means employed in the conversion of cluster density and velocity information into a simulated LOFAR radio sky are somewhat rudimentary given the uncertainties in the physics responsible for radio halos and the small scales on which it likely operates. However, our results are the first based on combining a large-scale cosmological gasdynamics simulation with observed features of radio halos, and they show that future simulations with higher resolution and more realistic physics should enable straightforward comparisons with results from low-frequency radio observatories. While earlier analytical studies have involved more sophisticated models of CR generation, such as including spectral steepening effects, these have relied on the X-ray luminosity function combined with the known correlation between radio power and X-ray luminosity (Enßlin & Röttgering 2002), the Press-Schechter mass function (Cassano et al. 2006), or Monte-Carlo realizations (Cassano 2010), whereas our work is based on direct access to the internal state of the simulated clusters. Donnert et al. (2010a) introduced a simulation of the Local Group including magnetic field injection and CR generation, but these results may be sensitive to the assumptions made about the magnetic field injection and are limited in volume. Our simulation, while involving simpler physics, covers a large ($1 \ h^{-1}$ Gpc) volume, which will allow us to gather reliable statistics and produce mock whole-sky radio maps, which are difficult to produce accurately with methods based on analytical mass functions.

In Section 2 we provide details of the cosmological simulation, while in Section 3 we explain the procedure used to associate a radio power with each cluster. We explore the range of valid models in Section 4 and use these results to produce radio power relations in Section 5. Section 6 discusses the results in terms of radio halo counts as functions of flux and redshift, and we present various example radio sky maps in Section 7. Finally, we conclude in Section 8 with a discussion of future directions.

2. THE SIMULATION

We simulated structure formation using the ΛCDM cosmological model within a periodic box spanning $1024 \ h^{-1}$ comoving Mpc. We assumed a Hubble constant $H_0 = 100h$ km s^{-1} Mpc^{-1} with $h = 0.719$, a present-day matter density parameter $\Omega_{m,0} = 0.262$, baryonic density parameter $\Omega_{b,0} = 0.0437$, vacuum density parameter $\Omega_{\Lambda,0} = 0.738$, and spatially flat geometry, as suggested by results from WMAP data (Komatsu et al. 2011). Initial conditions for 1024^3 dark matter particles at a starting redshift $z_i = 66$ were generated using a

version of GRAFIC (Bertschinger 2001) modified to accept power spectra generated by CMBFAST (Seljak & Zaldarriaga 1996). We normalized the power spectrum using $\sigma_8 = 0.74$. We included adiabatic gasdynamics for the baryons using a perfect-gas equation of state with adiabatic index $\gamma = 5/3$ and mean particle mass determined using interpolation from collisional ionization equilibrium tables for primordial gas from Sutherland & Dopita (1993). Although no additional physics is included in this first calculation, we initialized the gas temperature at z_i to a constant value of 9100 K, corresponding to a preheating entropy of 250 keV cm^2 at a redshift of 3. This level of preheating is adequate to reproduce the observed X-ray luminosity-temperature relation (Bialek et al. 2001) for clusters of galaxies, although details of the scatter in this relation and its correlation with other cluster properties such as the presence of cold cores are not constrained to match observations.

We ran our simulation using the FLASH code version 3.3 (Fryxell et al. 2000; Dubey et al. 2008) using a new direct multigrid Poisson solver (Ricker 2008) with 1024^3 dark matter particles and a uniform 1024^3 base mesh. The piecewise-parabolic method (Colella & Woodward 1984) was used to solve the Euler equations of gasdynamics. To achieve the resolution necessary to estimate the level of turbulence within clusters, we used adaptive mesh refinement within 100 preselected regions. Each region was 50 h^{-1} Mpc on a side centered on a halo identified using a lower-resolution precursor run. The halos were selected to uniformly sample the range of resolvable halos using mass function weighting to ensure a representative sample in the full simulation. Within the preselected regions we used a dark matter particle refinement criterion, allowing no more than 100 dark matter particles within a zone. We refined to a maximum resolution of 32 h^{-1} kpc. Estimates of the integral scale of turbulence in clusters suggests a power law spectrum from spatial scales of 0.8 to 8 kpc, with no visible turnover (Kuchar & Enßlin 2011), suggesting that the integral scale is larger than 8 kpc and that our resolution should allow us to determine the level of turbulent dissipation. Since the refined regions were larger than the halos on which they were centered, we captured a total of 131 high-resolution clusters. We ran the code on the Cray XT5 machine at Oak Ridge National Laboratory, where the simulation required approximately 450,000 CPU-hours on 16,000 processors. Output files containing both particle and gas information were written beginning at $z = 2.0$ at every $\Delta z = 0.25$ for the purposes of mock sky generation.

2.1. *Halo finding and virial mass*

We created halo catalogs from the simulation outputs using the friends-of-friends (FOF) technique with a linking length parameter $b = 0.2$ and considered only halos with at least $3,000$ particles (i.e. an FOF dark-matter mass of 2×10^{14} h^{-1} M$_\odot$). Our base-grid spatial resolution is sufficient to ensure accurate counts of halos with this many particles throughout the range of redshifts we consider here (Heitmann et al. 2005; Lukić et al. 2007). Figure 1 shows our mass function for all halos in the simulation volume compared against the best fit of Warren et al. (2006). We find fewer high-mass objects relative to the Warren fit, but this is not unexpected (see, for
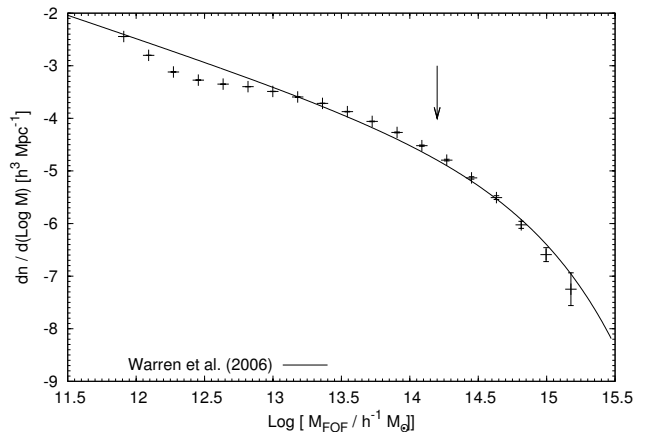

FIG. 1.— Mass function of all halos in the simulation volume compared against best fit of Warren et al. (2006). Errors bars are given at 2σ and the vertical arrow denotes our FOF halo completeness limit.

example, Knebe et al. 2011). Also, we tend to overproduce low mass objects, even below our resolvability limit. However, note that even though we produce too many low-mass objects relative to the Warren fit below our resolution limit, our mass function still turns away from the expected slope, and thus we cannot fully trust the number counts below this threshold. There were ~ 4000 resolvable objects at $z = 0.0$.

To make comparisons with the observational analysis of Cassano et al. (2006) (hereafter CBS06), we compute a spherical overdensity radius R_v for each of our halos. For the high-resolution sample (i.e., the adaptively-refined halos within the 100 predefined regions), we compute overdensities including both just dark matter and with dark matter plus gas. For the remaining fixed-resolution halos outside the predefined regions, we only include dark matter in the overdensity calculation since the gas data in these halos were poorly resolved. In Section 6 we discuss our procedure for assigning radio power to these lower-resolution halos. We use the same definition of overdensity as in CBS06, namely Kitayama & Suto (1996):

$$\Delta_c = 18\pi^2 \left(1 + 0.4093\omega(z)^{0.9052}\right), \qquad (1)$$

where $\omega(z) \equiv \Omega_f(z)^{-1} - 1$. Here,

$$\Omega_f = \frac{\Omega_{m,0}(1+z)^3}{\Omega_{m,0}(1+z)^3 + \Omega_\Lambda}. \qquad (2)$$

The virial mass, M_v, follows as $M_v = (4/3)\pi\Delta_c\rho_m(z)R_v^3$, where $\rho_m(z)$ is the mean mass density:

$$\rho_m(z) = 2.87 \times 10^{11}\Omega_{m,0}(1+z)^3 \; h^2 \; M_\odot \; \mathrm{Mpc}^{-3}. \quad (3)$$

The most massive cluster in our simulation has a mass $M_v = 1.2 \times 10^{15}$ h^{-1} M$_\odot$.

3. SIMULATING RADIO EMISSION

We identify gas zones within R_v for each halo and associate them with the halo in which they are found. We create two-dimensional maps of projected density and projected turbulent pressure, $m_i v_i^2$, where m_i is the mass in the cell i and the average velocity is defined as the difference between the measured velocity in the cell and the bulk velocity averaged over 300 kpc regions, $\mathbf{v}_i \equiv \mathbf{v}_i - \bar{\mathbf{v}}_{300 \; \mathrm{kpc}}$. This is a strategy for removing bulk

motions similar to Vazza et al. (2011) (an alternative approach to remove bulk velocities from this calculation is discussed in Paul et al. 2011). We use these projections in two ways: to create simulated surface brightness maps and to construct total radio luminosities by integrating these quantities across the entire projected cluster surface out to the virial radius. The integrated projected density is of course M_v and we will designate the integrated turbulent pressure as $\Gamma_v = \sum_i m_i v_i^2$.

Therefore we can create simulated radio surface brightness maps for our clusters by normalizing maps of projected turbulent pressure and projected mass using assumed radio luminosities and rest-frame spectra. Because we may not fully resolve intracluster turbulence, the total amount of turbulent pressure in our clusters may be lower than the $\sim 10\%$ of hydrostatic pressure seen in high-resolution simulations (Ricker & Sarazin 2001; Ritchie & Thomas 2002; Mitchell et al. 2009). However, because the normalization of the radio power is supplied independently (see below), all we require of the turbulent pressure maps is that they be sufficiently diffuse and representative in spatial extent of clusters containing radio halos. The detailed structure of the maps should not be regarded as realistic. Because of the beam smearing described below, this fact does not significantly affect our analysis. Also, while we cannot depend on these simulated clusters to provide correct high-resolution X-ray and radio surface brightness maps, we can still use them to identify broad features, such large-scale shocks and the relative radial dependence of turbulence.

Using these integrated quantities, we construct a rest frame 1.4 GHz radio power via

$$P_{1.4 \text{ GHz}} = C_s B_s M_v^a \Gamma_v^c, \tag{4}$$

where C_s is a scaling constant, M_v is the virial mass, Γ_v is the virial turbulent pressure, and B_s is the magnetic field parameter:

$$B_s = \frac{B(M_v)^2}{(B(M_v)^2 + B_{\text{CMB}}^2)^2}, \tag{5}$$

where $B(M_v) \equiv \langle B \rangle (M_v/\langle M \rangle)^b$ and $B_{\text{CMB}} \equiv 3.2(1 + z)^2 \ \mu$G is the equivalent magnetic field strength of the cosmic microwave background. This formulation separates physical processes that generate cosmic rays (M_v and Γ_v) from those that contribute to radio emission (B in the numerator) and CR losses due to emission (B^2 in the denominator) and inverse Compton scattering (B_{CMB}). The losses enter into this equation because they limit the maximum CR energy. In this formalism, M_v measures the total cluster mass and thus should scale with the dependence of cosmic ray generation on hadronic secondary processes, whereas Γ_v measures the total cluster turbulence and thus should provide a measure of the re-acceleration of cosmic ray electrons by that turbulence. We will set $\langle M \rangle = 1.5 \times 10^{15} \ M_\odot$. There are thus five independent parameters: the average magnetic field $\langle B \rangle$, the scaling of magnetic field with cluster mass, b, the scaling of radio power with virial mass, a, the scaling of radio power with turbulent pressure, c, and an overall scaling parameter C_s. A summary of our model parameters is given in Table 1.

This model is a generalization and extension of the one derived in Cassano & Brunetti (2005). Note that the analysis of hadronic secondary models of Dolag & Enßlin

TABLE 1
PARAMETERS OF THE RADIO LUMINOSITY MODEL.

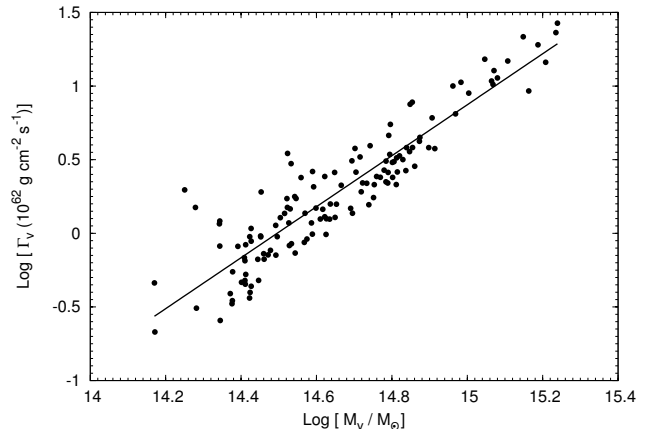| Parameter	Description
C_s	Overall scaling
$\langle B \rangle$	Average magnetic field
b	Scaling of magnetic field with cluster mass
a	Scaling of radio power with cluster mass
c	Scaling of radio power with turbulent pressure

FIG. 2.— Total turbulent pressure, Γ_v, versus virial mass, M_v at $z = 0$ for the high-resolution cluster sample. Shown is a best-fit line in log space. The slope of the line is ~ 1.7.

(2000) identified the functional form of the magnetic field as $B = B(M_v)^2/(B(M_v)^2 + B_{\text{CMB}}^2)$, i.e. the denominator is not squared. Our model easily accommodates this scenario: when B_{CMB} dominates, this will appear as a constant factor folded into C_s, and when $B(M_v)$ dominates this will simply adjust the mass scaling factor a. We are fixing the form of the magnetic field dependence since the radio synchrotron power will always depend on magnetic field pressure (B^2) independently of the cosmic ray generation and acceleration mechanisms (see Cassano & Brunetti (2005) for a discussion). We stress that although this model is relatively simple and ignores the streaming and diffusion of cosmic rays (Enßlin et al. 2011), it allows us to explore a range of plausible acceleration mechanisms and examine relative changes to luminosity functions, scaling relations, and other radio properties.

This model allows us to explore both cosmic ray generation mechanisms or a mixture of both. For example, the hadronic secondaries model should predict radio power which scales with cluster mass, so $c = 0$ in this case. A re-acceleration model is proportional to turbulent pressure, so a would be 0. Note that the model of CSB06 is based on re-acceleration, but only scales with cluster mass. This is because Γ_v roughly scales with M_v with a logarithmic slope of 1.7, as shown in Figure 2. There is some scatter in this relation due to the merger history of a particular cluster: recent mergers produce stronger levels of turbulence, which tend to scatter the cluster higher in this relation. Note that the model of CSB06 corresponds here to $a = 4/3$ and $c = 0$.

A degeneracy exists for calculations of total radio luminosity between models that scale with turbulent pressure and those that scale with mass, since we may freely exchange c for $1.7a$ and vice-versa. However, a more de-

tailed examination of cluster atmospheres reveals striking differences. Even with the relatively low resolution of our simulation, and the resulting inability to fully reproduce correct structures in the cluster atmospheres, we can identify gross differences in the projected maps. Figure 3 shows projections of mass and turbulent pressure for two clusters. The mass projections of both clusters are roughly spherical, as expected. However, the turbulent pressure maps show more varying morphology. While the halos are roughly equal in mass ($\sim 8 \times 10^{14}\ h^{-1}\ \mathrm{M}_\odot$), one shows much greater turbulent structure, indicating recent merger activity, which may explain the scatter in Figure 2. Thus, even though different mechanisms of CR generation may produce similar cluster counts (as we will see below), high-resolution radio and X-ray imaging of clusters may help to determine which mechanism dominates.

Since we do not include in our simulations any detailed cosmic ray generation mechanisms, and we because we want to keep our model as general as possible, we must fix the scaling parameter C_s by using observations. This scaling will then combine any extra constants and parameters not included in our analysis. For a given set of model parameters, we set C_s by assigning a radio luminosity to the most massive cluster in our simulation. This cluster has a mass $\sim 3 \times 10^{15}\ h^{-1}\ \mathrm{M}_\odot$, which fits within the observed radio halo mass range of $2 \times 10^{15} - 6 \times 10^{15}\ h^{-1}\ \mathrm{M}_\odot$. We do this with the $P_{1.4} - M_v$ relation found in CBS06, which is based on combining the observed correlation of radio halo power and X-ray luminosity with the correlation between X-ray luminosity and mass:

$$
\begin{aligned}
&\log\left[\frac{P_{1.4}}{3.16 \times 10^{24} h_{70}^{-1} \mathrm{W\ Hz^{-1}}}\right] = \\
&(2.9 \pm 0.4) \log\left[\frac{M_v}{10^{15}\ h_{70}^{-1}\ \mathrm{M}_\odot}\right] - (0.814 \pm 0.147)
\end{aligned}
\tag{6}
$$

We then apply this same constant scaling to all remaining high-resolution halos in the sample. While the scaling may contain some additional dependence on mass or turbulent pressure not accounted for in our parameterization, this can easily be accommodated in our study by adding to (or subtracting from) the parameters a and c. An example of a particular model compared against the observed relation is shown in Figure 4. Our best-fit relation in this plot and throughout this paper uses only the clusters within the observed mass range.

Since no radio halos have been observed beyond a redshift of ~ 0.4, and available statistics do not strongly constrain evolution in this relation, we will fix the scaling at $z = 0$ and apply the same scaling to higher-redshift clusters. We will also assume power-law energy spectra with a spectral index of 1.2, consistent with low-redshift observations (Feretti et al. 2004). Finally, we do not include in our model the relationship between synchrotron break frequency and the presence of a radio halo, which can be used to calibrate models to the observed fraction of clusters hosting radio halos (CBS06). We will discuss the potential impacts of this assumption in the conclusion.

4. EXPLORATION OF VALID MODELS

To constrain our model choices we make selections for the model parameters, assign radio powers to the clusters using the procedure described above, find the best fit line to our derived $P_{1.4} - M_v$ data above a mass threshold of $10^{15}\ h^{-1}\ \mathrm{M}_\odot$, and compare the best-fit slope and normalization to the observed values. We only accept model choices that produce fits that lie within 1σ of the observed relation. This is a strategy similar to the one employed by CBS06, but that we are applying a slightly more stringent test by enforcing the known relation to somewhat lower radio powers than they consider. We do this so that we can capture enough halos (~ 10) to generate sufficient statistics for our best-fit lines. Obviously, we could just select two models that span the valid range and analyze their difference, but we wish to explore the relationships among the various model parameters and the separate consequences of varying each one.

Figure 5 shows colormap plots of allowable models. We vary $\langle B \rangle$ from 0.2 to 6.0 μG, b from 0.5 to 1.5, a from 0.0 to 5.0, and finally c from 0.0 to 3.0. We could explore even larger values of a and c, but as we will discuss below 1σ uncertainties in the measured $P_{1.4\mathrm{GHz}} - M_v$ relation place upper limits on the scaling of a and c at these chosen maximum values. We also assume a positive correlation between radio power and M_v and Γ_v. While we allow the mass and turbulent pressure scaling parameters to vary all the way to 0, we constrain the scalings associated with magnetic fields. We constrain the average cluster magnetic field strength from 0.2 μG, which is set by observed upper limits on hard X-ray emission (CBS06), to 6.0 μG, which is a reasonable upper limit from rotation measure observations (e.g. Govoni et al. 2004; Bonafede et al. 2011). The restrictions on b come from the simulations of Dolag et al. (2002), which followed the adiabatic compression of seed magnetic fields as clusters formed. They found a scaling $B \propto M^{1.33}$. We allow some uncertainty in this value, but do not allow a compete lack of scaling of magnetic field with cluster mass. For simplicity, we have combined the mass and turbulent pressure values as $a + c$, so $a + c$ is varied from 0.0 to 9.0. The contours for each individual parameter show structures similar to those for this combined parameter. In these plots we are showing the *maximum* allowed value for a given point on each contour plot. All values less than the plotted value are also allowed. For example, for $b = 1.0$ and $\langle B \rangle = 3.0\ \mu$G the allowable values for $a + c$ are from 0.0 to ~ 1.5.

We find that very strong magnetic fields are only allowed if the scalings with virial mass and turbulent pressure are very steep. In these cases strong radio power in low mass objects due to high $\langle B \rangle$ is offset by significantly lower radio power associated with M_v or Γ_v. If the scaling of magnetic field strength with cluster mass is above unity, then it is difficult to fit strong magnetic fields at high mass within the observed relations. We find several regions forbidden in our models: strong magnetic fields coupled with low $a + c$, and very low or very high $a + c$ and b values.

We see interesting structures in the contours: steps and wiggles in the $a + c$ plots, and striations in the others. These are due to the scatter that develops in the $P_{1.4} - M_v$ relations and the resulting variations of the best fit lines. Because of this variation, we do not see monotonically increasing (or decreasing) behavior in the contour plots, especially at extreme values. Surprisingly, we find that $a = c = 0.0$ is allowed, but only at low $\langle B \rangle$ and high b. This is because of the implicit mass de-
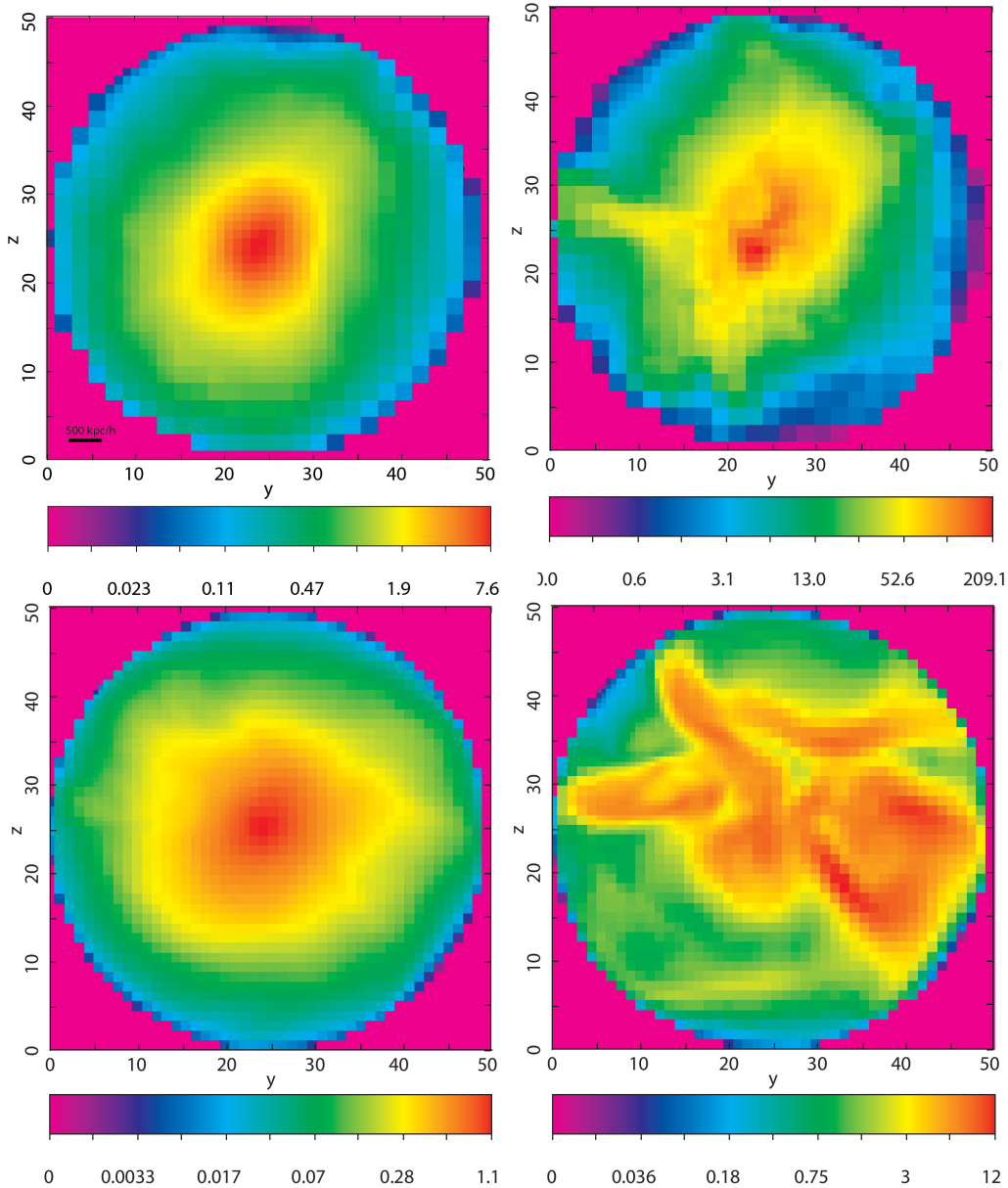
Fig. 3.— Projected density (left-hand plots) and projected turbulent pressure (right-hand plots) for a two clusters (top and bottom rows). Projections are taken along the x-direction within R_v for each cluster. The units for projected density are 10^{44} g cm^{-2} and for projected turbulent pressure are 10^{58} g s^{-2}. The images are normalized to a uniform grid 50 cells on a side. The corresponding comoving length scale is indicated in the figure.

pendence in the calculation of the cluster magnetic field strength, $B(M_v)$. Also, the model used in CBS06 is *forbidden* in our analysis, since we are enforcing the known relation to a wider range of cluster masses. However, we can allow their model choice when restricting ourselves to the mass ranges they consider.

We use these contours to guide our selection of models for further study. We wish to adequately sample the space of allowable models and explore the limits allowed by observational constraints. We also wish to explore the effects of holding one parameter constant and varying the others to their extreme allowed values. To aid analysis, we collect our choices into six model groups, enumerated in Table 2. In this table we list the values chosen for a particular parameter set and a unique designation for that set used in further plots.

In Model Group 1 we set a to 0.0, fix $c = 0.7$, and

vary the magnetic field parameters as widely as possible from a minimum of $\langle B \rangle = 0.2$ to 3.1 μG. We also vary the scaling parameter associated with the magnetic field, b. Each $\langle B \rangle$ is coupled with a unique b, except for $\langle B \rangle = 1.5$ μG, where we examine $b = 0.8$ and $b = 1.1$, which are the minimum and maximum allowed values for this particular configuration. We explore the opposite behavior in Model Set 2 by fixing the magnetic field parameters to $\langle B \rangle = 2.0$ μG and simple linear scaling $b = 1.0$ while having no explicit M_v dependence and studying the maximum and minimum allowed values for turbulent pressure scaling, c. We chose this value of the magnetic field so that we could get the maximum difference in c. We keep the same magnetic field configuration for Model Set 3, but here we exchange a and c using the measured relation (Figure 2). In this Model Set we fix the quantity $a + 2c$. This allows us to hold the magnetic
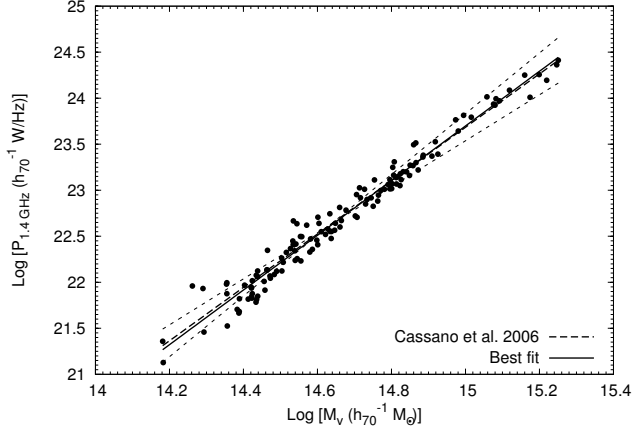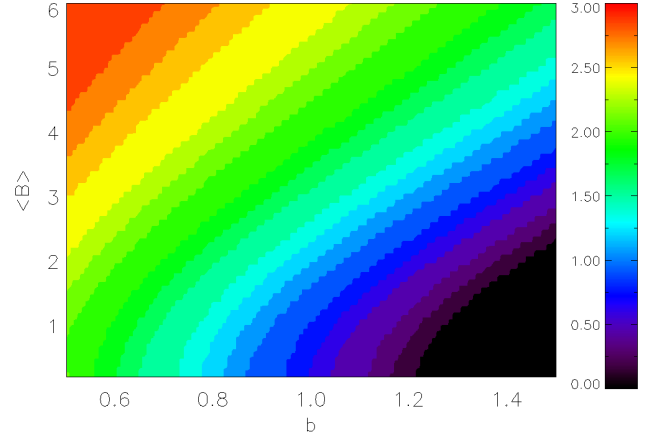
FIG. 4.— Radio halo luminosity versus virial mass for one example model (points) with best fit above 10^{15} h^{-1} $M_{\odot}$ (solid line) compared against the observed best fit found in CBS06 (thick dashed line) and 1σ uncertainties (thin dashed lines). Points are the high-resolution cluster sample. The example uses parameters $\langle B \rangle = 2.0$ μG, $b = 1.0$, $a = 0.0$, and $c = 0.7$.
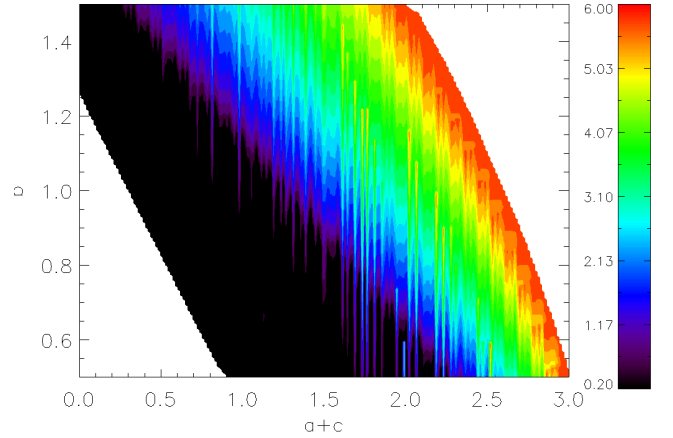
TABLE 2
MODEL GROUPS AND PARAMETER SETS.

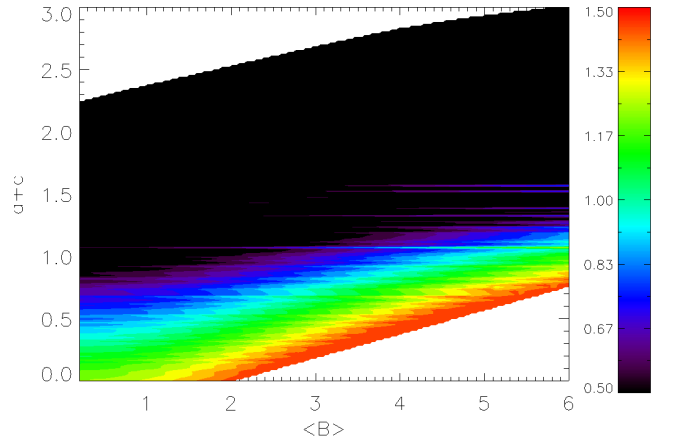| Designation	$\langle B \rangle (\mu G)$	b	a	c
Model Group 1) Fixed c, Varying Magnetic Field				
1A	0.2	0.650	0.000	0.700
1B	0.5	1.000	0.000	0.700
1C	1.5	0.800	0.000	0.700
1D	1.5	1.100	0.000	0.700
1E	3.1	1.470	0.000	0.700
Model Group 2) Fixed Magnetic Field				
2A	2.0	1.000	0.000	0.510
2B	2.0	1.000	0.000	0.930
Model Group 3) Exchanging a and c				
3A	2.0	1.000	1.300	0.000
3B	2.0	1.000	0.650	0.325
3C	2.0	1.000	0.000	0.650
Model Group 4) Extreme Allowed Magnetic Fields, Fixed c				
4A	0.2	1.000	0.000	0.700
4B	3.1	1.000	0.000	0.700
Model Group 5) Extreme Allowed Magnetic Fields				
5A	0.2	0.500	0.000	0.875
5B	6.0	1.500	2.000	0.000
Model Group 6) Extreme Allowed Scalings				
6A	0.2	1.260	0.000	0.010
6B	6.0	0.600	0.000	1.550

field fixed while going from a hadronic-like CR model ($c = 0$) to a re-acceleration model ($a = 0$). We designed this Model Set to verify that our results are robust to even exchanges of a and c using the measured relation, which they should be. In Model Set 4 we fix $b = 1.0$, $a = 0.0$, and $c = 0.7$ and examine the extreme allowed average magnetic field. We chose these values of b, a, and c such that we could get the maximum change in $\langle B \rangle$. We repeat this test in Model Set 5, but now allow b, a, and c to vary to accommodate the extreme val-

(a) $a + c$ as a function of $\langle B \rangle$ and b.

(b) $\langle B \rangle$ as a function of b and $a + c$.

(c) b as a function of $a + c$ and $\langle B \rangle$.

FIG. 5.— Contours of allowed radio halo model parameters. Allowed models are determined by fitting a line to our $P_{1.4} - M_v$ data above M^{15} h^{-1} $M_{\odot}$ and ensuring that the slope and normalization are within 1σ of the known relation. $\langle B \rangle$ is given in units of μG.

ues studied of $\langle B \rangle$. Finally in Model Set 6 we pick two model parameter sets that represent extremes of all four parameters.

5. RADIO POWER RELATIONS

We begin our analysis by using our sample of 131 high-resolution clusters to examine the relationship between radio luminosity and virial mass and X-ray luminosity. To construct X-ray luminosities, we use the `mekal` plasma emissivity model supplied with the XSPEC package (Arnaud 1996). We then build a composite X-ray spectrum for each cluster and use that spectrum to generate the $0.1 - 2.4$ keV rest-frame luminosity within the spherical radius R_v for each cluster. Since our simulation does not include cooling and central AGN feedback, our cluster temperatures, and hence X-ray luminosities, are uniformly higher than observed (see Stanek et al. (2010) for a discussion of such effects). However, the slopes of our relations are still within observed limits, and we can still study the relative differences among models and their evolution with redshift.

In Figure 6 we show the best-fit slope and normalization for each model, grouped by model group, for the $P_{1.4} - M_v$ relation generalized from (Eq. 6):

$$\log \left[\frac{P_{1.4}}{3.16 \times 10^{24} h_{70}^{-1} \text{W Hz}^{-1}} \right] = A_f \log \left[\frac{M_v}{10^{15} \ h_{70}^{-1} \ \text{M}_\odot} \right] + b_f$$
(7)

where A_f and b_f (note that we have added the suffix f for "fit" to distinguish these from the parameters used in our radio power model) are the slope and normalization, respectively. We fix the scaling parameter C_s at each redshift for each model. In essence this assumes that the $P_{1.4\text{GHz}} - M_v$ relation holds even at high redshift. For each model we show three points: one each for $z = 0.0, 0.25,$ and 0.5. Above redshift 0.5 we do not have enough halos above the minimum mass threshold to generate meaningful statistics. Note that the observational uncertainties essentially fill the entire plotting space.

For Model Group 1, where we vary only the magnetic field parameters, we see a progressive steepening of the slope with higher b values, as expected. Note especially the differences between models 1C and 1D, which have identical values of $\langle B \rangle$. The values of b and $\langle B \rangle$ also jointly affect the normalization of the $P_{1.4\text{GHz}} - M_v$ relation, with smaller values b generally leading to lower normalizations. The redshift evolution of the models in this Model Group shows diverse behavior. For models with $b < 1.0$ the normalization tends decreases with increasing redshift, but not very significantly. This makes sense as the clusters are in general uniformly smaller at higher redshift. However, the slope increases at $z = 0.25$, which perhaps suggests greater variance in the turbulent properties of the clusters. The uncertainties in the values for redshifts 0.25 and 0.5 make them difficult to compare against each other. With $b > 1.0$, the trend reverses and the normalization tends to increase with high redshift.

In Model Group 2, where we keep the magnetic field fixed and vary the scaling with turbulent pressure, we see that, as expected, larger values of c lead to steeper slopes and lower normalizations in the best fit relation. Since our scatter is related to the turbulent pressure, models with higher values of c will have correspondingly larger uncertainties. We see similar redshift dependence

for model set 2A as in Model Group 1, but the model set 2B displays reverse behavior (increasing normalization with redshift), although the uncertainties are so large as to make firm statements difficult. The steep dependence on turbulent pressure overwhelms the general mass dependence, so that even though the clusters are in general smaller at higher redshift (leading to a lower normalization), the turbulence in the most massive cluster (which is used to fix the normalization) increases, negating the mass effect.

For Model Group 3 we see that exchanging a for c in the radio power model does lead to small differences in the slope and normalization. When we set $c = 0$ (so that there is no dependence on turbulent pressure) we essentially eliminate the uncertainties. The small differences are due to the fact that our scaling relation between Γ_v and M_v is only a best-fit approximation, and that scatter in that relation can affect the resulting $P_{1.4\text{GHz}} - M_v$ relation. All the points, however, are within 2σ of each other. All these models show identical redshift dependence.

We see the drastic effects of changing the assumed average magnetic field in Model Group 4. Higher magnetic fields lead to higher normalizations and flatter slopes. However, the redshift evolutions exhibit opposite trends, such that at $z = 0.5$ the effects of the magnetic field are indistinguishable from each other. For weak magnetic fields, the cosmic rays are dominated by their interactions with the CMB, and the equivalent pressure of the CMB increases with redshift, lowering the synchrotron power at higher z. For strong fields, the dependence on cluster mass is more explicit, and at higher redshifts the clusters are, in general, smaller and the mass distribution has a steeper slope.

In Model Group 5 we see that the dependence on the scalings overwhelms the dependence on the average magnetic field. Even though model set 5A has the same $\langle B \rangle$ as set 4A, the dependence on b, a, and c forces a much flatter slope. Thus we may conclude that the effects of average magnetic field are degenerate with the scaling parameters, although the parameters taken individually can lead to significant differences. Similar behaviors are displayed by Model Group 6, although the error bars are so small because of the weak dependence on the turbulent pressure.

In Figure 7 we repeat the above analysis for the $P_{1.4} - L_x$ relation:

$$\log \left[\frac{P_{1.4}}{3.16 \times 10^{24} h_{70}^{-1} \text{W Hz}^{-1}} \right] = A_f \log \left[\frac{L_x}{10^{45} h_{70}^{-1} \text{ergs s}^{-1}} \right] + b_f.$$
(8)

We find similar behaviors as in the $P_{1.4\text{GHz}} - M_v$ relation plots above, except that our error bars are generally larger due to scatter from our estimates of L_x. Since X-ray luminosities are generally easier than virial masses to compute from observations, observations of many more radio halos may reduce the statistical uncertainties to such a level as to potentially distinguish the allowed scalings and dependencies. The redshift evolution of the $P_{1.4} - L_x$ relation especially may provide a way of determining the dominant components of radio power and the average magnetic strength of clusters, as we have discussed above for the $P_{1.4} - M_v$ relation..

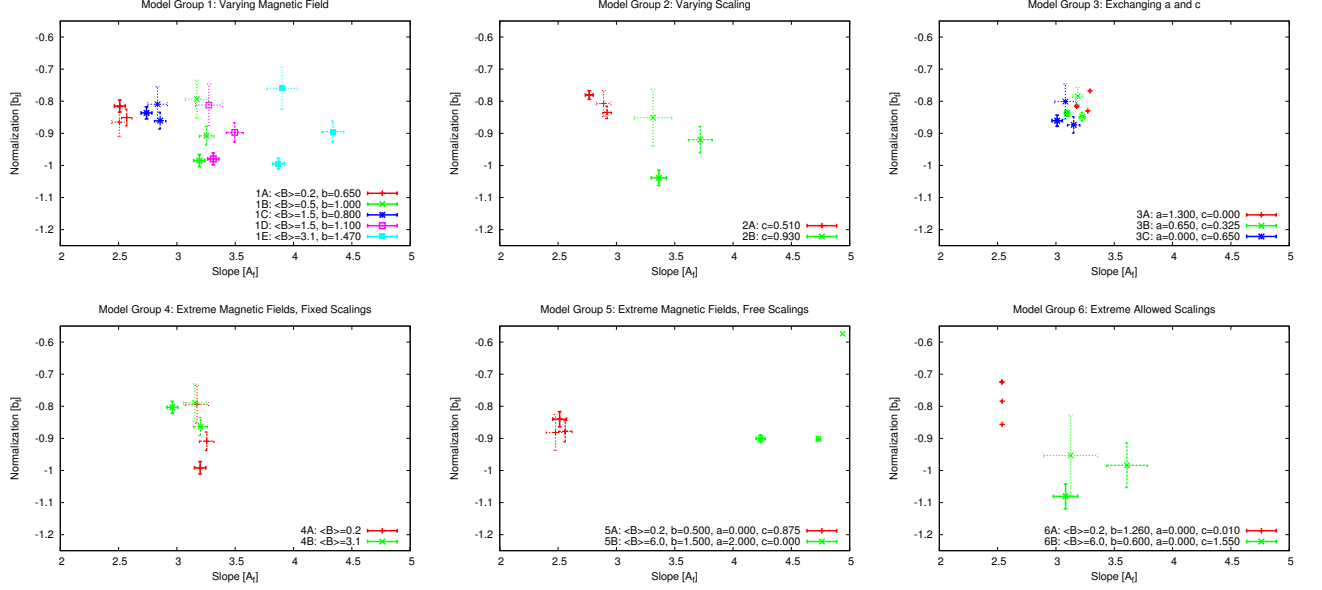In general, if the observational uncertainties in A_f and

FIG. 6.— Best fits for the $P_{1.4} - M_v$ relation for each radio halo parameter set. Each best fit to Eq. 7 generates a slope and normalization, which we represent as a point with 1σ error bars. Solid lines are the best fit at $z = 0.0$, thick dashed lines are $z = 0.25$, and thin dashed lines are $z = 0.5$. We have identified each model with its designation from Table 2 and the portions of the model that change in the given model group. $\langle B \rangle$ is given in units of μG.
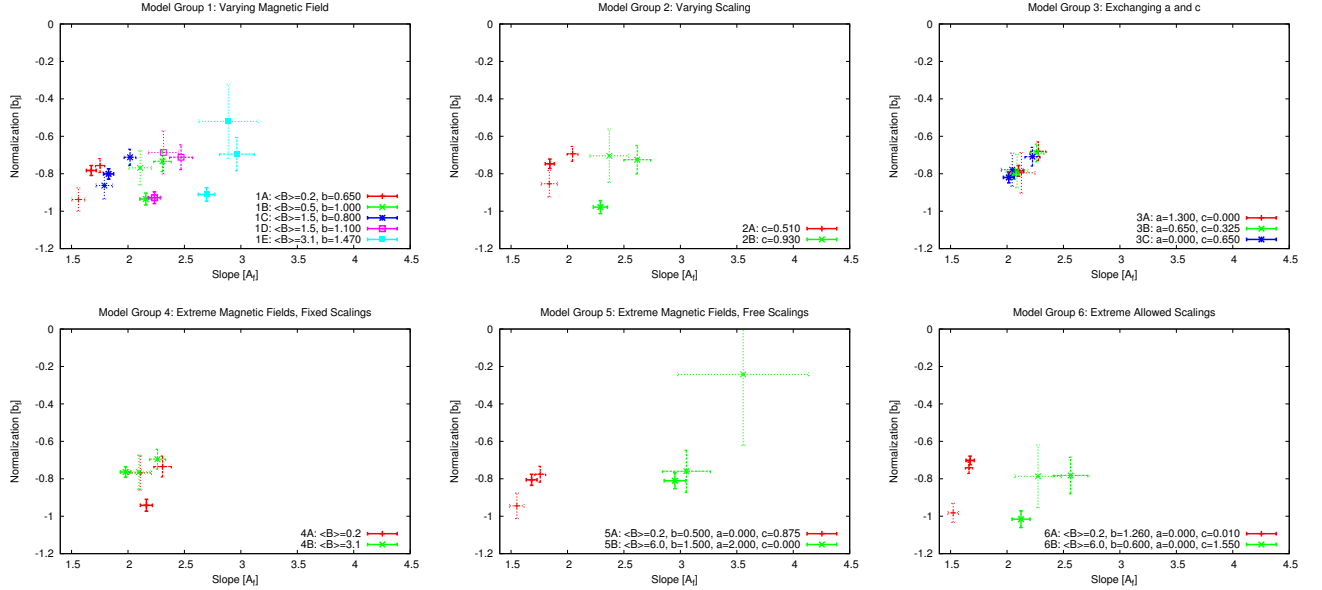

FIG. 7.— Best fits for the $P_{1.4} - L_x$ relation for each radio halo parameter set. Methods and colors are identical to Figure 6. We have identified each model with its designation from Table 2 and the portions of the model that change in the given model group. $\langle B \rangle$ is given in units of μG.

b_f are reduced by approximately a factor of two, many degeneracies in the model parameters will be eliminated. We note that we are basing this analysis on our sample of only 131 clusters. While this is significantly more than the current known number of radio halos, it is still far fewer than we expect to see with instruments such as LOFAR, as we will see below. While more objects could reduce the uncertainty, the precise amount of error also depends on the intrinsic scatter in the observed relations, which can be affected by biases. We also assume a power-law relationship holds between radio power and cluster mass even to low-mass clusters, which may not be the case once significant numbers of low-luminosity halos are detected.

6. LUMINOSITY FUNCTIONS AND RADIO HALO COUNTS

We now turn to a discussion of these models in terms of total counts of all objects in the simulation. To do this, we must assign a rest-frame radio luminosity to each cluster in the simulation box, even if it is not at high resolution. We accomplish this by combining the derived $\Gamma_v - M_v$ relations described above with a relationship between M_v, which includes gas, and $M_{v,\mathrm{DM}}$, which only includes dark matter. Our smallest clusters are only a few zones across and thus do not contain enough gas zones to accurately capture the contribution of the gas
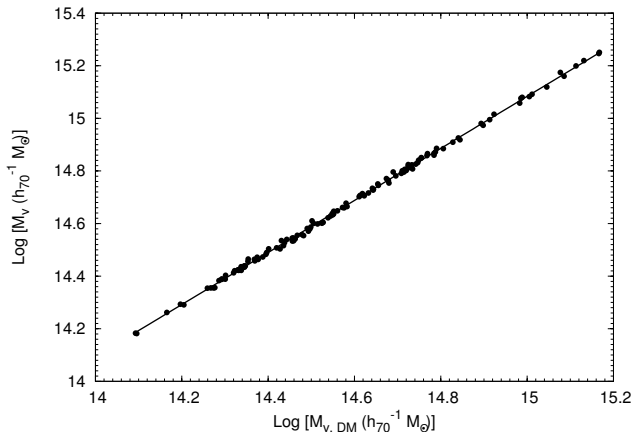
FIG. 8.— Data for (points) and best fit to (solid line) the M_v - $M_{v,\mathrm{DM}}$ relation. Points are the high-resolution cluster sample.

to M_v. However, we defined our FOF halo completeness limit so that we can always get reliable evaluations of $M_{v,\mathrm{DM}}$ (i.e., $R_v \geq \Delta x$, where Δx is the resolution of our pre-refinement uniform grid). This gives us an interpolated value of Γ_v for each fixed-resolution cluster, which we then feed into Eq. 4 to generate a radio power for that cluster.

We find a very tight correlation between M_v and $M_{v,\mathrm{DM}}$ for our high-resolution sample, as shown in Figure 8. We fit a line to these data and found the correlation to be

$$\log\left[\frac{M_v}{10^{15}\ h_{70}^{-1}\ \mathrm{M_\odot}}\right] = 0.99\log\left[\frac{M_{v,\mathrm{DM}}}{10^{15}\ h_{70}^{-1}\ \mathrm{M_\odot}}\right] + 0.08.$$

(9)

This relationship implies a uniform gas fraction consistent with other simulations (e.g., Stanek et al. 2010). We use this fit to extract an M_v for each fixed-resolution cluster (i.e., those outside the refinement regions) which is then used to compute its equivalent radio power using the $\Gamma_v - M_v$ relation. While equivalent to directly interpolating from a $\Gamma_v - M_{v,\mathrm{DM}}$ relation, we found that this procedure produces less scatter and hence more reliable interpolations. We do *not* add additional scatter to the interpolation procedure. For the analysis below we will include Poissonian uncertainty where appropriate, and this dwarfs any uncertainty introduced by scatter. By binning our data for luminosity functions, the main effect of scatter is to simply move clusters around within a given luminosity bin, and any clusters that are scattered into a luminosity bin are roughly offset by clusters scattered out of the same bin, especially at low luminosities where the function is relatively flat.

Not every cluster hosts a radio halo, and for simplicity we will only assign radio halos to 5% of our clusters. This is roughly in line with observations, which indicate that $\sim 1/3$ of clusters above $2 \times 10^{15}\ h^{-1}\ \mathrm{M_\odot}$ and only $2-5\%$ of smaller clusters host radio halos (Cassano et al. 2008). We do this rather than employing a radio halo probability that is a step function in mass because we do not have enough high-mass ($> 10^{15}\ h^{-1}\ \mathrm{M_\odot}$) halos to calibrate our number counts based on the intrinsic scatter in our derived $P_{1.4\mathrm{GHz}} - M_v$ relation. Note that in the context of hadronic secondary models, this enforced fraction implies that not every cluster is sufficiently magnetized to generate radio emission. More sophisticated

techniques to calibrate number counts exist, such as using the synchrotron break frequency, ν_b, which is used in the identification of radio halos (see CBS06 for a discussion). However, again we do not have enough high-mass objects to use this approach. With enough high-mass halos, the precise calibration would depend on our choice of parameters $\langle B \rangle$, b, a, and c. Thus we may be overcounting the number of radio halos at 1.4 GHz. However, we can still gather useful results as to the relative effects of varying radio halo models. Also, our analysis will include results at 150 MHz, where ν_b is much lower and hence our results are more valid. To calculate the radio luminosity at 150 MHz, we assume a simple power law with spectral index 1.2. Our smallest resolvable cluster has a 1.4 GHz radio luminosity of $\sim 2 \times 10^{21}\ \mathrm{W\ Hz^{-1}}$.

Figure 9 shows our calculated radio halo luminosity functions at redshift $z = 0.0$ at 1.4 GHz and 150 MHz. At high masses our luminosity function is well below the estimated values of Enßlin & Röttgering (2002). However, this is not unexpected due to our limited simulation volume and cosmic variance, and the fact that they assume a Press-Schechter mass function with a fixed $1/3$ fraction of clusters hosting radio halos. For Model Group 1, in which we fix the dependence on cluster mass and turbulent pressure but vary the average magnetic field strength and scaling of magnetic field with cluster mass, we see a bifurcation in the luminosity function at low luminosities: models with $b < 1.0$ produce up to a factor of two more low-luminosity radio halos than those models with $b > 1.0$. The distinction is much more significant at 150 MHz, where more objects allow for smaller uncertainties (assuming perfect detector sensitivity — a point which we will address later in the discussion of number counts). However, despite difference in the $P_{1.4\mathrm{GHz}} - M_v$ relations, models 1A and 1C are largely indistinguishable from each other, as are models 1B, 1D, and 1E. Number counts at low luminosity are reduced significantly when the magnetic field scaling b is greater than unity.

We see in Model Group 2, in which we keep the magnetic field values fixed, that steeper scalings with turbulent pressure produce many fewer radio halos at both 1.4 GHz and 150 MHz. The models at 1.4 GHz are only statistically distinguishable at the lowest luminosities, but the models at 150 MHz are easily separable throughout almost the entire range of radio luminosities. Similar conclusions can be made regarding Model Group 4, which brackets the extreme allowed magnetic fields with fixed scalings, where strong differences in the assumed average magnetic field strength lead to somewhat distinguishable differences. These behaviors persist for Model Groups 5 and 6, in which all parameters are allowed to vary, with the general rule being that it is difficult to separate these models when only relying on 1.4 GHz halo counts. The only models that remain inseparable are those in Model Group 3, in which our exchanges of a and c lead to degenerate radio halo counts at both frequencies, as expected.

To accumulate total and binned counts we set a vantage point in the center of our computational domain and find halos whose locations lie on the light cone emanating from this position. To do this we use saved checkpoint files at $z = 0.0, 0.25, 0.5, 0.75,$ and 1.0. Moving outwards in small ($\Delta z = 0.05$) redshift slices covering the same range, we locate the nearest output (in redshift)
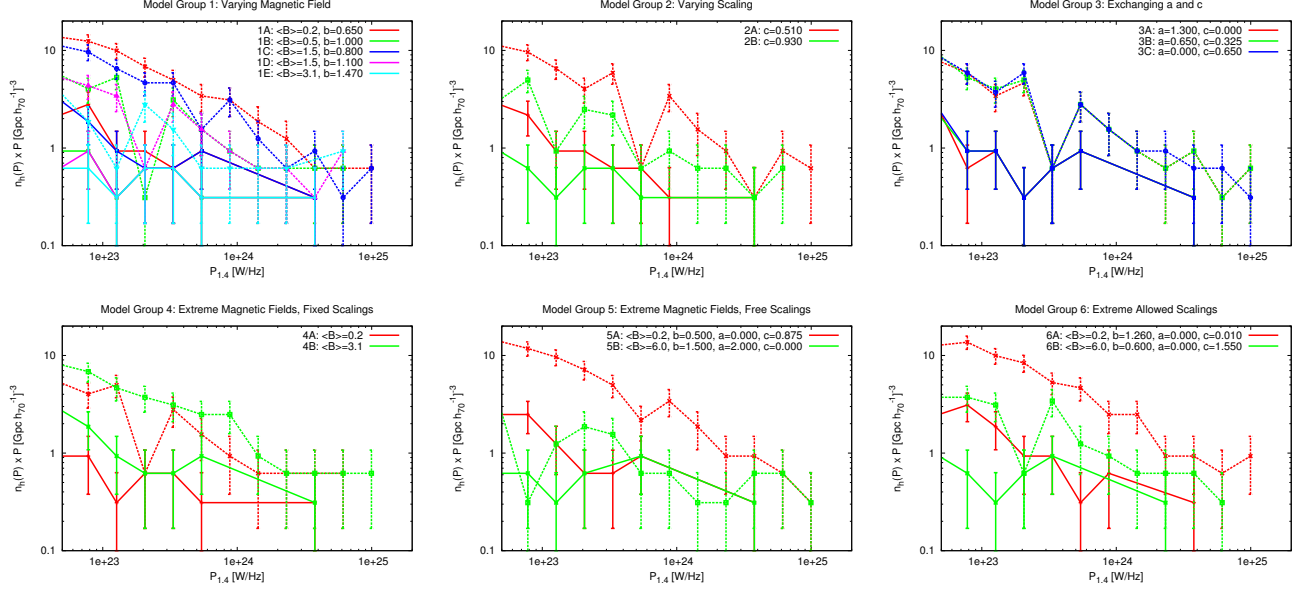
FIG. 9.— Radio halo luminosity functions at $z = 0.0$. Solid lines are luminosity functions at 1.4 GHz and dashed lines are at 150 MHz. Error bars indicate 1σ Poisson uncertainties. We have identified each model with its designation from Table 2 and the portions of the model that change in the given model group. $\langle B \rangle$ is given in units of μG.

to each slice and use the center-of-mass peculiar velocities of the clusters found in that output to estimate new positions in the slice under consideration. We then compute the flux as $P/(4\pi d_L^2)$, where d_L is the luminosity distance of the cluster. We do this at both 1.4 GHz and 150 MHz assuming a spectral index of 1.2.

We begin with Figure 10, where we show the total counts of radio halos at 1.4 GHz and 150 MHz in the observable universe as a function of flux limit in mJy. To generate error bars we propagate the 1σ uncertainties in the derived M_v - $M_{v,\mathrm{DM}}$ and $\Gamma_v - M_v$ fits to generate a minimum and maximum radio power for each cluster. Our number counts are bound by the resolvability limit of our simulation. While the model trends continue from the above analysis, we find that at high flux limits (> 100 mJy) and high frequencies, we have too few radio halos to strongly distinguish several models, even those with large discrepancies in either assumed average magnetic field or scalings with virial mass or total turbulent pressure. This is due to the suppression of radio halos at high redshift, meaning that the integrated counts depend most strongly on high-luminosity objects, where the counts are nearly the same. At 150 MHz and an assumed LOFAR sensitivity limit of 30 mJy, we find that although some models, such as model sets 2A and 2B, produce an almost factor of two difference in the total counts, the large uncertainties preclude any clean distinction.

In Figure 11 we show the total counts of radio halos within redshift $z < 0.2$ at 1.4 GHz and 150 MHz. This redshift range fits largely within our computational volume without the need for periodic replication of the domain and is more easily accessible to observers. Although we find little degradation in the total number counts in the LOFAR-accessible regime (> 30 mJy), the models remain indistinguishable.

7. SIMULATED RADIO SKY MAPS

While we could in principle produce mock sky maps within any frequency range, we choose LOFAR-like parameters since low-frequency instruments are able to survey large portions of the sky and hence collect many halo images for use in statistical comparison. We generate raw mock sky maps in the $20 - 240$ MHz LOFAR bandpass by following a similar strategy of interpolating and redshift-correcting clusters as used above. Appropriate cosmological dimming and redshift are then applied to determine the contribution of the slice to the sky observed at $z = 0$. We generate a radio image for each cluster by projecting its density and turbulent pressure onto the skymap and computing the relevant radio intensity using a given set of radio model parameters, ensuring that the integrated radio power across the projected cluster is equal to the value obtained using M_v and Γ_v in the above sections. We only project gas values within R_v. For halos not within the high-resolution sample, we identify the nearest high-resolution cluster in mass and copy that high-resolution image to the location of the low-resolution halo. While this procedure is admittedly somewhat crude, it does allow us to explore some of the observational consequences of these models and demonstrates a method of generating radio maps in the future using more sophisticated and realistic simulated data.

Figure 12 shows the entire radio sky containing our simulated clusters at 120 arcsecond resolution assuming no background (i.e., a threshold sensitivity of 0 mJy). This resolution best approximates the LOFAR beam at an average frequency of ~ 120 MHz and a longest baseline of $L \sim 2$ km. For this example we have chosen model parameter set A1. This map particularly highlights the paucity of radio halos in the universe, even at low sensitivity thresholds, but it is useful for providing a mock all-sky map for linking simulations to observations.

Figure 13 highlights a region of the sky 6 degrees on a side at a resolution of 10 arcseconds, representing the high-resolution capability between 20 and 240 MHz at the longest baseline configuration of LOFAR. We also
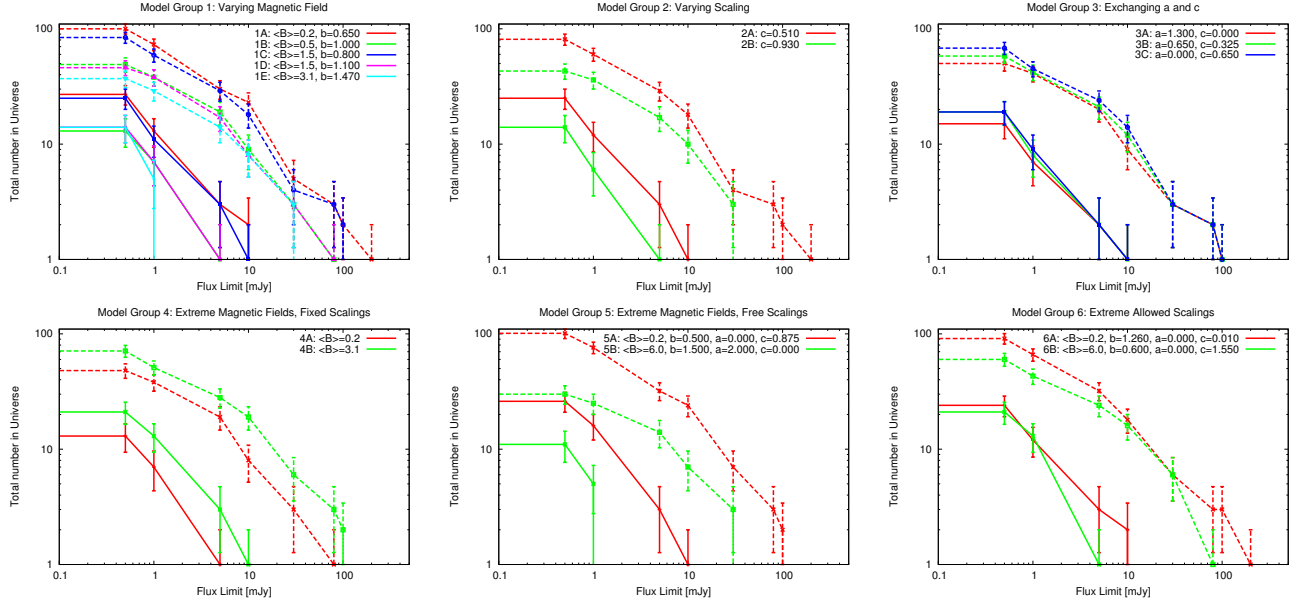
FIG. 10.— Radio halo total counts at 1.4 GHz (solid lines) and 150 MHz (dotted lines) versus flux limit in mJy. Error bars indicate 1σ Poisson uncertainties. We have identified each model with its designation from Table 2 and the portions of the model that change in the given model group. $\langle B \rangle$ is given in units of μG.
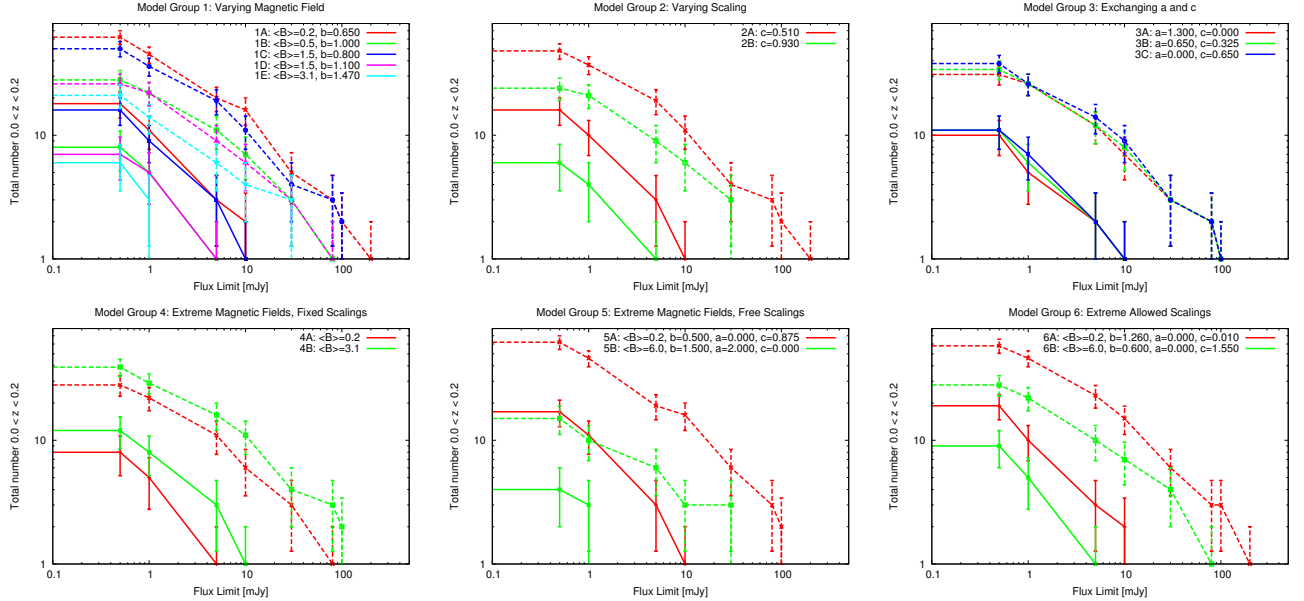

FIG. 11.— Radio halo counts for $z < 0.2$ at 1.4 GHz (solid lines) and 150 MHz (dotted lines) versus flux limit in mJy. Error bars indicate 1σ Poisson uncertainties. We have identified each model with its designation from Table 2 and the portions of the model that change in the given model group. $\langle B \rangle$ is given in units of μG.

draw contour levels at varying sensitivities: 1, 10, and 30 mJy. These sensitivities represent different configurations of the LOFAR array. At high resolution and peak sensitivity, we are able to clearly distinguish several substructures and features within the two radio halos, indicating that LOFAR may be able to cleanly distinguish various radio power models based on their dependence on local gas density or local turbulent pressure, which can have different characteristic structures in the cluster atmosphere (Figure 3). At lower sensitivities, we can still distinguish features in the cluster cores, and early LOFAR images of nearby and bright radio halos may also provide useful distinguishing results. We will present a detailed radio morphological study, which re-

quires knowledge of the spatial dependence of the magnetic field, in a future paper.

Figure 14 shows the same region of the sky as above with a much lower resolution of of 240 arcseconds. The contours are the same as above. While we lose significant information about distant and small clusters, some larger clusters, such as the one shown, still show significant structure even at lower resolutions. We see that we can still identify substructure within the large cluster, and the effects of higher sensitivity thresholds are limited to distant clusters and the outer regions of nearby objects. These results are encouraging, since they indicate that LOFAR may be able to give detailed radio maps of many radio halos.
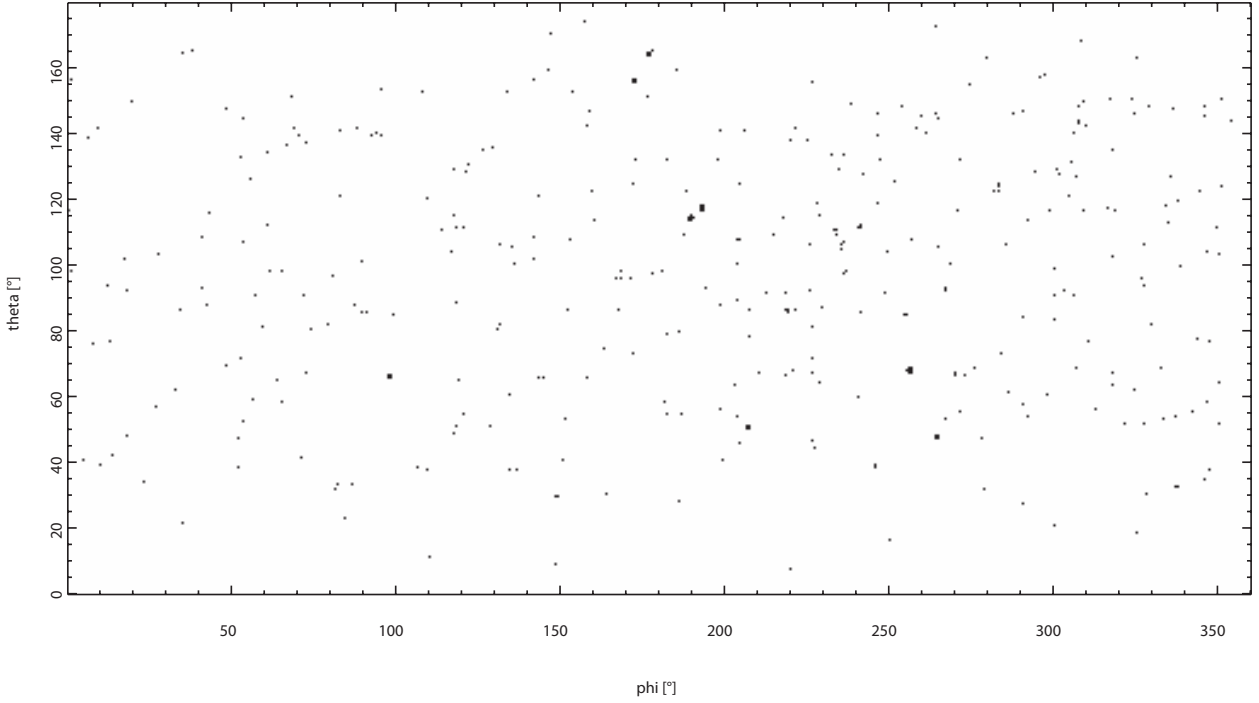
Fig. 12.— Example radio halo all-sky map. This map assumes 0 mJy sensitivity threshold and a resolution of 120 arcseconds.
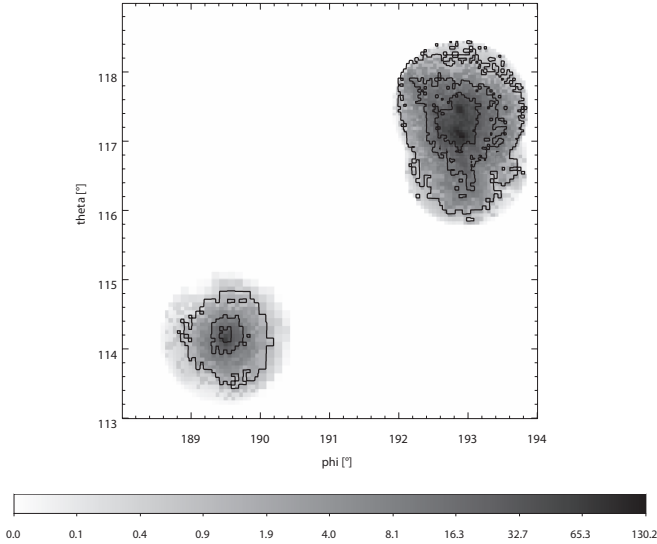

Fig. 13.— Example radio halo partial-sky map at 10 arcsecond resolution. The color scale is the logarithm of radio power in mJy. Contours are drawn at 1, 10, and 30 mJy levels.
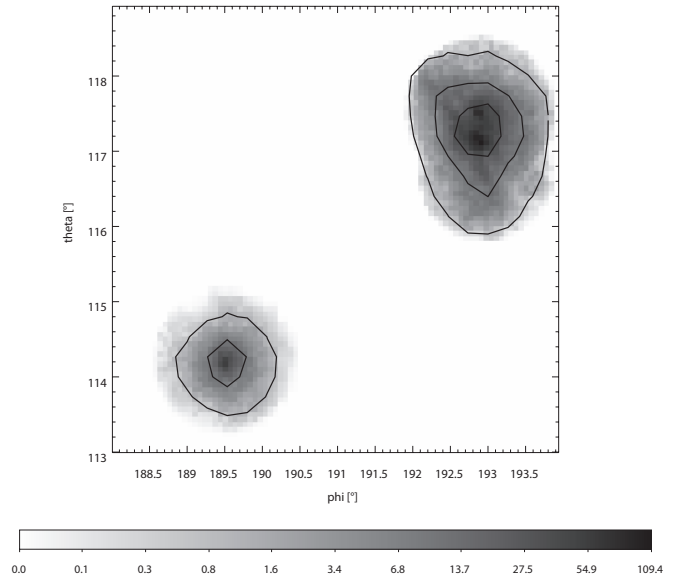

Fig. 14.— Example radio halo partial-sky maps at 240 arcsecond resolution. The color scale is the logarithm of radio power in mJy. Contours are drawn at 1, 10, and 30 mJy levels

8. CONCLUSIONS

We have introduced the first set of radio halo statistics derived entirely from large-scale cosmological simulation. Our radio power model is sufficiently broad to encompass many viable and more realistic models of cosmic ray generation and synchrotron emission in clusters of galaxies. Our approach demonstrates the viability of using large-scale simulation to bridge simulations and observations, both by deriving radio halo statistics from the simulated data to constrain possible radio power models and by producing mock radio sky maps that can be directly compared to observations.

From our analysis we have determined that the slope

and normalization of the $P_{1.4\text{GHz}} - M_v$ and $P_{1.4} - L_x$ relations are potentially key probes of the various models of cosmic ray generation. They also allow us to place limits on the average cluster magnetic field strength and the scaling of magnetic fields with cluster mass. With the uncertainties from only 131 observed radio halos we can significantly constrain the scaling of radio power with cluster mass and turbulent pressure. With the 131 objects of our high-resolution sample we are able to clearly separate some models with strong statistical significance. The evolution with redshift of these relations also allows us to potentially distinguish various models. Future low-frequency missions, which will surveys large portions of the sky, may then potentially capture enough objects to perform a similar analysis and obtain these constraints.

Our limited volume prevents us from counting the very largest — and hence rarest — clusters. However, we predict an order of magnitude fewer high-frequency radio halos at low mass (where the undercounting effects of our simulation volume are negligible) than the analysis of CSB06 and Cassano et al. (2010). Some of this discrepancy might be due to our lack of steep-spectrum halos, which get counted via inclusion of the calculation of the synchrotron break frequency, ν_b. Instead, we just assign a radio halo to 5% of our clusters. However, we found that adjusting the spectral index to 1.9 (i.e., the average spectral index found by Cassano et al. 2010) only increased the number counts by roughly 50%, which is not nearly enough to explain the differences. The analytical estimates of CSB06 may be over-estimating the level of turbulence in the intracluster medium, whereas our simulations provide direct access to the cluster dynamical state. On the other hand, our approach of refining only cells but not dark matter particles may somewhat limit our dynamic range in the clusters, leading to an underestimate of the turbulence (although we agree with other, better-resolved simulations). This issue will be more carefully examined in subsequent work.

We have uncovered many degeneracies among the scalings of radio power with cluster mass and turbulent pressure and the mass-dependence of cluster magnetic fields. These degeneracies can be broken by several methods. For example, a better understanding of the relationship between cluster mass and magnetic field will constrain our $\langle B \rangle$ and b parameters, allowing us to make more conclusive statements about the observational limits placed upon the a and c parameters. On the other hand, more high-resolution radio and X-ray images of clusters may constrain the effectiveness of the various mechanisms of generating cosmic rays, which would further constrain our a and c parameters. In particular, measurements of intracluster gas velocities (such as may be possible with future X-ray spectroscopic missions) would enable mapping of the projected turbulent pressure, which could then be compared with the projected mass distribution.

We find that low-frequency surveys are potentially capable of distinguishing and constraining the scaling of radio power with cluster mass and turbulent pressure, since the radio halo number counts are much higher at lower frequencies. Even though low-frequency surveys have relatively low sensitivity, their ability to map large portions of the sky to moderately high redshift means that they can gather many more objects than high-frequency (and more sensitive) observations. However, our estimates indicate that LOFAR will only see on the order of 10 radio halos within our studied mass range, and that future missions with more sensitivity will be required in order to cleanly distinguish models. Future radio observations are especially important since the gamma ray emission associated with the production of cosmic rays from hadronic secondary interactions from clusters might be too small for Fermi to detect, which means that we may not be able to use this instrument to distinguish models (Brunetti 2009).

Similarly, since hadronic secondary models of cosmic ray production are highly degenerate with re-acceleration models when only considering total counts and integrated cluster quantities, high-resolution low-frequency radio images are required in order to effectively distinguish these models. Although high-frequency observations can also (and do) produce similar maps, surveys such as LOFAR have the unique capability of capturing many such images, potentially providing a statistically significant means of distinguishing models based on morphological differences. Our simulated radio cluster and sky maps are freely available upon request to the authors or via the project website [1] under the section `Projects/RadioHaloMaps`. We have produced images at a variety of sky coverage areas, sensitivity limits, and resolutions for all of the models described above. These images are simple `FITS` files. The images are straightforward to produce, allowing us to explore further refinements to the models and more sophisticated instrument modeling.

Since this initial work is highly preliminary, we have room for many improvements and modifications to make stronger connections with observations. As an immediate improvement we may perform simulations with larger volumes than our 1 h^{-1} Gpc box (or, equivalently, perform multiple realizations of the same volume) in order to capture more massive objects. With larger volumes we can also capture more low- and moderate-mass objects to obtain better statistics for the $P_{1.4\text{GHz}} - M_v$ and other relations. These simulations will allow us employ more sophisticated models of cosmic ray generation and evolution as well as enable us to calculate statistics of radio halo morphologies. With more simulations, we may begin to investigate the dependence of radio halo counts on cosmological parameters. We may also begin to self-consistently include magnetic fields, although our results in this approach would be tied to a specific model of magnetic field injection and growth. Similarly, we can begin to investigate generating and propagating cosmic rays in the simulation, although it is difficult to scale current methods to large volumes and high resolutions. Since the expected low-luminosity radio halo number counts are so sensitive to the level of turbulence in cluster atmospheres, we must incorporate more careful techniques for estimating this. However, our results demonstrate an important first step in bridging simulations and observations to more fully understand the large-scale radio universe.

---

[1] http://sipapu.astro.illinois.edu/

REFERENCES

Ackermann, M. et al. 2010, ApJ, 717, L71

Arnaud, K. A. 1996, in Astronomical Society of the Pacific Conference Series, Vol. 101, Astronomical Data Analysis Software and Systems V, ed. G. H. Jacoby & J. Barnes, 17

Bacchi, M., Feretti, L., Giovannini, G., & Govoni, F. 2003, A&A, 400, 465

Bertschinger, E. 2001, ApJS, 137, 1

Bialek, J. J., Evrard, A. E., & Mohr, J. J. 2001, ApJ, 555, 597

Blasi, P. 1999, Astropart. Phys., 12, 169

Blasi, P. & Colafrancesco, S. 1999, Astroparticle Physics, 12, 169

Bonafede, A., Govoni, F., Feretti, L., Murgia, M., Giovannini, G., & Brueggen, M. 2011, arXiv:1103.0277

Brunetti, G. 2009, Magnetic Fields in the Universe II: From Laboratory and Stars to the Primordial Universe (Eds. A. Esquivel), 36, 201

Brunetti, G., Cassano, R., Dolag, K., & Setti, G. 2009, A&A, 507, 661

Brunetti, G. & Lazarian, A. 2011, MNRAS, 410, 127

Brunetti, G., Venturi, T., Dallacasa, D., Cassano, R., Dolag, K., Giacintucci, S., & Setti, G. 2007, ApJ, 670, L5

Brunetti, G. et al. 2008, Nature, 455, 944

Buote, D. A. 2001, ApJ, 553, L15

Cassano, R. 2010, A&A, 517, A10

Cassano, R. & Brunetti, G. 2005, MNRAS, 357, 1313

Cassano, R., Brunetti, G., Röttgering, H. J. A., & Brüggen, M. 2010, A&A, 509, A68

Cassano, R., Brunetti, G., & Setti, G. 2006, MNRAS, 369, 1577

Cassano, R., Brunetti, G., Venturi, T., Setti, G., Dallacasa, D., Giacintucci, S., & Bardelli, S. 2008, A&A, 480, 687

Cohen, A. S., Lane, W. M., Cotton, W. D., Kassim, N. E., Lazio, T. J. W., Perley, R. A., Condon, J. J., & Erickson, W. C. 2007, AJ, 134, 1245

Colella, P. & Woodward, P. 1984, Journal of Computational Physics, 54, 174

Deiss, B. M., Reich, W., Lesch, H., & Wielebinski, R. 1997, A&A, 321, 55

Dennison, B. 1980, ApJ, 239, L93

Dolag, K., Bartelmann, M., & Lesch, H. 2002, A&A, 387, 383

Dolag, K. & Enßlin, T. A. 2000, A&A, 362, 151

Donnert, J., Dolag, K., Brunetti, G., Cassano, R., & Bonafede, A. 2010a, MNRAS, 401, 47

Donnert, J., Dolag, K., Cassano, R., & Brunetti, G. 2010b, MNRAS, 407, 1565

Donnert, J., Dolag, K., Lesch, H., & Müller, E. 2009, MNRAS, 392, 1008

Dubey, A., Reid, L. B., & Fisher, R. 2008, Physica Scripta, T132, 014046

Enßlin, T., Pfrommer, C., Miniati, F., & Subramanian, K. 2011, A&A, 527, A99

Enßlin, T. A. & Röttgering, H. 2002, A&A, 396, 83

Feretti, L., Brunetti, G., Giovannini, G., Kassim, N., Orrú, E., & Setti, G. 2004, Journal of Korean Astronomical Society, 37, 315

Fryxell, B. et al. 2000, ApJS, 131, 273

Giovannini, G. 1999, New Astronomy, 4, 141

Giovannini, G., Bonafede, A., Feretti, L., Govoni, F., Murgia, M., Ferrari, F., & Monti, G. 2009, A&A, 507, 1257

Giovannini, M. 2009, Phys. Rev. D, 79, 121302

Govoni, F., Markevitch, M., Vikhlinin, A., VanSpeybroeck, L., Feretti, L., & Giovannini, G. 2004, ApJ, 605, 695

Heitmann, K., Ricker, P. M., Warren, M. S., & Habib, S. 2005, ApJS, 160, 28

Jaffe, W. J. 1977, ApJ, 212, 1

Jarvis, M. J. 2007, At the Edge of the Universe: Latest Results from the Deepest Astronomical Surveys ASP Conference Series, 380, 251

Jeltema, T. E. & Profumo, S. 2011, ApJ, 728, 53

Kempner, J. C., Blanton, E. L., Clarke, T. E., Enßlin, T. A., Johnston-Hollitt, M., & Rudnick, L. 2004, Proceedings of The Riddle of Cooling Flows in Galaxies and Clusters of Galaxies (arXiv:astro-ph/0310263)

Kempner, J. C. & Sarazin, C. L. 2001, ApJ, 548, 639

Keshet, U. & Loeb, A. 2010, ApJ, 722, 737

Kitayama, T. & Suto, Y. 1996, ApJ, 469, 480

Knebe, A. et al. 2011, MNRAS, 415, 2293

Komatsu, E. et al. 2011, ApJS, 192, 18

Kuchar, P. & Enßlin, T. A. 2011, A&A, 529, A13

Kuo, P.-H., Hwang, C.-Y., & Ip, W.-H. 2004, ApJ, 604, 108

Large, M. I., Mathewson, D. S., & Haslam, C. G. T. 1959, Nature, 183, 1663

Li, H., Lapenta, G., Finn, J. M., Li, S., & Colgate, S. A. 2006, ApJ, 643, 92

Liang, H., Hunstead, R. W., Birkinshaw, M., & Andreani, P. 2000, ApJ, 544, 686

Lukić, Z., Heitmann, K., Habib, S., Bashinsky, S., & Ricker, P. M. 2007, ApJ, 671, 1160

Mitchell, N. L., McCarthy, I. G., Bower, R. G., Theuns, T., & Crain, R. A. 2009, MNRAS, 395, 180

Paul, S., Iapichino, L., Miniati, F., Bagchi, J., & Mannheim, K. 2011, ApJ, 726, 17

Petrosian, V. 2001, ApJ, 557, 560

Pfrommer, C., Enßlin, T. A., & Springel, V. 2008, MNRAS, 385, 1211

Ricker, P. M. 2008, ApJS, 176, 293

Ricker, P. M. & Sarazin, C. L. 2001, ApJ, 561, 621

Ritchie, B. W. & Thomas, P. A. 2002, MNRAS, 329, 675

Röttgering, H. 2003, New Astronomy Reviews, 47, 405

Röttgering, H. J. A. et al. 2006, eprint arXiv:astro-ph/0610596

Russell, H. R., van Weeren, R. J., Edge, A. C., McNamara, B. R., Sanders, J. S., Fabian, A. C., Baum, S. A., Canning, R. E. A., Donahue, M., & O'Dea, C. P. 2011, MNRAS, L297

Schlickeiser, R., Sievers, A., & Thiemann, H. 1987, A&A, 182, 21

Seljak, U. & Zaldarriaga, M. 1996, ApJ, 469, 437

Stanek, R., Rasia, E., Evrard, A. E., Pearce, F., & Gazzola, L. 2010, ApJ, 715, 1508

Sutherland, R. S. & Dopita, M. A. 1993, ApJS, 88, 253

Vazza, F., Brunetti, G., Gheller, C., Brunino, R., & Brüggen, M. 2011, A&A, 529, A17+

Warren, M. S., Abazajian, K., Holz, D. E., & Teodoro, L. 2006, ApJ, 646, 881

Wolfe, B., Melia, F., Crocker, R. M., & Volkas, R. R. 2008, ApJ, 687, 193